

The GAPS programme at TNG

XXXIV. Activity-rotation, flux–flux relationships, and active-region evolution through stellar age^{★,★★}

J. Maldonado¹, S. Colombo¹, A. Petralia¹, S. Benatti¹, S. Desidera², L. Malavolta³, A. F. Lanza⁴, M. Damasso⁵, G. Micela¹, M. Mallonn⁶, S. Messina⁴, A. Sozzetti⁵, B. Stelzer^{7,1}, K. Biazzo⁸, R. Gratton², A. Maggio¹, D. Nardiello^{2,9}, G. Scandariato⁴, L. Affer¹, M. Baratella⁶, R. Claudi², E. Molinari¹⁰, A. Bignamini¹¹, E. Covino¹², I. Pagano⁴, G. Piotto³, E. Poretti^{13,14}, R. Cosentino¹⁴, and I. Carleo^{15,2}

¹ INAF - Osservatorio Astronomico di Palermo, Piazza del Parlamento 1, 90134 Palermo, Italy
e-mail: jesus.maldonado@inaf.it

² INAF – Osservatorio Astronomico di Padova, vicolo dell’Osservatorio 5, 35122 Padova, Italy

³ Dipartimento di Fisica e Astronomia Galileo Galilei, Vicolo Osservatorio 3, 35122 Padova, Italy

⁴ INAF – Osservatorio Astrofisico di Catania, Via S. Sofia 78, 95123, Catania, Italy

⁵ INAF – Osservatorio Astrofisico di Torino, Via Osservatorio 20, 10025 Pino Torinese, Italy

⁶ Leibniz-Institute for Astrophysics Potsdam (AIP), An der Sternwarte 16, 14482, Potsdam, Germany

⁷ Institut für Astronomie und Astrophysik, Eberhard-Karls Universität Tübingen, Sand 1, 72076, Tübingen, Germany

⁸ INAF – Osservatorio Astronomico di Roma, Via Frascati 33, 00078, Monte Porzio Catone (Roma), Italy

⁹ Aix-Marseille Univ, CNRS, CNES, LAM, 13000 Marseille, France

¹⁰ INAF – Osservatorio Astronomico di Cagliari and REM, Via della Scienza 5, 09047 Selargius CA, Italy

¹¹ INAF – Osservatorio Astronomico di Trieste, Via Tiepolo 11, 34143 Trieste, Italy

¹² INAF – Osservatorio Astronomico di Capodimonte, Salita Moiariello 16, 80131 Napoli, Italy

¹³ INAF – Osservatorio Astronomico di Brera, Via E. Bianchi 46, 23807 Merate, Italy

¹⁴ Fundación Galileo Galilei - INAF, Rambla José Ana Fernandez Pérez 7, 38712 Breña Baja, Spain

¹⁵ Astronomy Department, 96 Foss Hill Drive, Van Vleck Observatory 101, Wesleyan University, Middletown, CT 06459, USA

Received 18 February 2022 / Accepted 19 April 2022

ABSTRACT

Context. Active-region evolution plays an important role in the generation and variability of magnetic fields on the surface of lower main sequence stars. However, determining the lifetime of active-region growth and decay as well as their evolution is a complex task. Most previous studies of this phenomenon are based on optical light curves, while little is known about the chromosphere and the transition region.

Aims. We aim to test whether or not the lifetime of active-region evolution shows any dependency on stellar parameters, particularly stellar age.

Methods. We identified a sample of stars with well-defined ages via their kinematics and membership to young stellar associations and moving groups. We made use of high-resolution échelle spectra from HARPS at La Silla 3.6-m-telescope and HARPS-N at TNG to compute rotational velocities, activity levels, and emission excesses. We used these data to revisit the activity-rotation-age relationship. The time-series of the main optical activity indicators, namely Ca II H and K, Balmer lines, Na I D₁, D₂, and He I D₃, were analysed together with the available photometry using state-of-the-art Gaussian processes to model the stellar activity of these stars. Autocorrelation functions of the available photometry were also analysed. We used the derived lifetimes of active-region evolution to search for correlations with stellar age, spectral type, and activity level. We also used the pooled variance technique to characterise the activity behaviour of our targets.

Results. Our analysis confirms the decline of activity and rotation as a star ages. We also confirm that the rotation rate decays with age more slowly for cooler stars and that, for a given age, cooler stars show higher levels of activity. We show that F- and G-type young stars also depart from the inactive stars in the flux–flux relationship. The Gaussian process analysis of the different activity indicators does not seem to provide any useful information on the lifetime and evolution of active regions. On the other hand, the lifetimes of active regions derived from the light-curve analysis might correlate with stellar age and temperature.

Conclusions. Although we suggest caution because of small number statistics, our results suggest that active regions seem to live longer on younger, cooler, and more active stars.

Key words. stars: activity – stars: chromospheres – stars: rotation

* Tables C.1 to C.3 are only available at the CDS via anonymous ftp to cdsarc.u-strasbg.fr (130.79.128.5) or via <http://cdsarc.u-strasbg.fr/viz-bin/cat/J/A+A/663/A142>

** Based on observations made with the Italian Telescopio Nazionale Galileo (TNG) operated by the Fundación Galileo Galilei (FGG) of the Istituto Nazionale di Astrofisica (INAF) at the Observatorio del Roque de los Muchachos (La Palma, Canary Islands, Spain).

1. Introduction

The relationships among stellar activity, rotation, and stellar age in solar-type stars have been widely studied. Chromospheric activity and rotation are linked by the stellar dynamo, and as the star evolves during the main sequence phase, it loses angular momentum via magnetic braking, and both rotation and activity diminish (e.g. Schatzman 1962; Kraft 1967; Weber & Davis 1967; Skumanich 1972; Noyes et al. 1984; Kawaler 1989; Soderblom et al. 1991; Jianke & Collier Cameron 1993; Montesinos et al. 2001; Barnes 2007; Mamajek & Hillenbrand 2008).

Active region (AR) growth and decay is another phenomenon related to the surface magnetic activity of solar-type stars with convective outer layers. The study of ARs is fundamental to improving our knowledge of the generation of magnetic fields and their variability. However, few studies have dealt with the analysis of AR lifetimes. In a series of papers, Donahue et al. (1997a,b) used the pooled variance technique on calcium data to infer the AR lifetimes of approximately 100 lower main sequence stars. The authors show that ARs have rather irregular lifetimes and that different stars might show very different pooled variance diagrams depending on their level of activity (age) and colour (mass).

More recently, several works have developed a methodology based on the decay of the autocorrelation function of light curves (in particular using data from the *Kepler* mission) to put constraints on starspots and AR lifetime. Giles et al. (2017) find that big starspots live longer irrespective of the spectral type of the star and that starspots decay more slowly on cooler stars. Santos et al. (2021) and Basri et al. (2022) discuss the effect of differential rotation and how it can destroy the biggest ARs, leading to a shorter AR lifetime. It is important to note that these works are based on optical light curves and therefore their conclusions refer to AR evolution in the stellar photosphere. However, it is well known that solar ARs in the chromosphere and in the transition region have lifetimes that are four to five times longer than those of the ARs in the solar photosphere.

Therefore, a detailed and homogeneous analysis of the chromospheric activity indexes of a large sample of stars with reliable age estimates is needed before possible mechanisms for AR growth and decay are invoked. This is the goal of this paper, in which we take advantage of the high number of high-resolution spectra taken within the framework of current radial-velocity planet searches to derive – in a homogeneous way – the time-series of the main optical activity indexes for a large sample of stars in open clusters and stellar associations with precise age estimates. Photometry time series from the TESS mission are also available for some of these stars. In addition, we take advantage of Gaussian processing, a state-of-the-art statistical analysis, to model stellar activity.

This paper is organised as follows. We present our stellar sample in Sect. 2. Section 3 describes the analysis of the data while in Sect. 4 we use our dataset to revisit the activity, rotation, and age relationships. The dependency of AR lifetime on spectral type, activity, and stellar age is discussed in Sect. 5 and we present our conclusions in Sect. 6.

2. Stellar sample

The sample analysed in this work is composed of 130 stars in open clusters or stellar associations with precise derived ages. The bulk of the sample is formed by stars observed within the framework of the Global Architecture of Planetary Systems

Table 1. Number of observed stars per cluster or moving group.

Association	N stars	Age (Myr)	Ref.
Taurus	4	1–2	(a)
Upper Sco	4	10	(b)
Cepheus	2	10–20	(c)
β Pic	2	24	(d)
Tucana – Horologium	4	30	(e)
Pleiades	2	112	(f)
AB Dor	2	149	(g)
Castor	1	200	(h)
Hercules – Lyra	1	257	(i)
Ursa Major	6	414	(j)
Coma Berenices	6	562	(k)
Praesepe	20	578	(l)
Hyades	49	750	(m)
Other young stars	2	50–600	(n,o)
NGC 752	12	1340	(p)
Old stars	13	5300–13 900	(q)
Sun		4579 ^(†)	(r)

References. (a) Kenyon & Hartmann (1995); (b) Pecaú & Mamajek (2016); (c) Klutsch et al. (2020); (d) Bell et al. (2015); (e) Torres et al. (2008); (f) Dahm (2015); (g) Bell et al. (2015); (h) Barrado y Navascués (1998); (i) Eisenbeiss et al. (2013); (j) Jones et al. (2015); (k) Silaj & Landstreet (2014); (l) Delorme et al. (2011); (m) Brandt & Huang (2015); (n) Carleo et al. (2021); (o) this work; (p) Agüeros et al. (2018); (q) Mamajek & Hillenbrand (2008); (r) Baker et al. (2005). ^(†)Minimum age.

programme (GAPS, Covino et al. 2013). In particular, 25 stars were selected from the GAPS Young Objects Project, a radial-velocity survey designed to probe the frequency of planets around young stars (Carleo et al. 2020). These 25 stars include young stars in well-known star forming regions (e.g. the Taurus complex with an age of ~ 2 Myr) as well as bona-fide members of open clusters and moving groups (such as Coma Ber or Ursa Major, age ~ 400 –600 Myr). An additional 48 stars were taken from the GAPS Open Cluster Project, a monitoring of selected stars in three open clusters (namely the Hyades, M44, and NGC 752) designed to study the relation between the physical properties of the planets and those of their host stars as well as the connection between the physical properties of the cluster environments and those of the planetary systems residing within them (Malavolta et al. 2016). Finally, 56 star members of clusters and moving groups or with well-known ages were selected from Mamajek & Hillenbrand (2008, hereafter MH08). Table 1 lists the number of stars by open cluster or kinematic group, while the corresponding Hertzsprung-Russell (HR) diagram of the observed stars is shown in Fig. 1.

The stars are required to have high-resolution HARPS-N (Cosentino et al. 2012) or HARPS (Mayor et al. 2003) optical échelle spectra. The instrumental setup of HARPS and HARPS-N is almost identical. The spectra cover the ranges 378–691 nm (HARPS) and 383–693 nm (HARPS-N) with a resolving power of $R \sim 115\,000$. The spectra are provided already reduced using HARPS-N/ESO standard calibration pipelines (Data Reduction Software, DRS version 3.7 and 3.8, respectively) and were retrieved from the corresponding ESO¹ and TNG² archives. In

¹ http://archive.eso.org/wdb/wdb/adp/phase3_spectral/form?

² <http://archives.ia2.inaf.it/tng/>

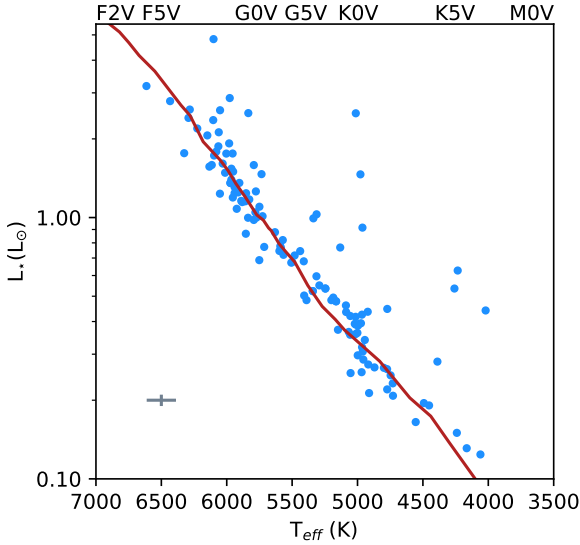


Fig. 1. Luminosity versus T_{eff} diagram for the observed stars. The red line shows the main sequence from Pecaut & Mamajek (2013).

addition, several solar spectra taken by the HARPS-N solar telescope (Dumusque et al. 2021) were analysed in order to use the Sun as a benchmark.

3. Analysis

3.1. Kinematics and age

Stellar age is one of the most difficult stellar parameters to constrain in an accurate way. Solar-type stars evolve too slowly to be dated by their position in the HR diagram. Membership to stellar associations and kinematic groups has been proposed as a way to overcome this difficulty and used as a methodology to identify young stars and to assign ages, especially after the release of the HIPPARCOS data. Today, the exquisite precision of the recently released *Gaia* EDR3 catalogue (Gaia Collaboration 2020) allows us to compute precise Galactic spatial-velocity components (U, V, W) and detailed probabilities of membership to young stellar associations.

Galactic spatial-velocity components were computed from the radial velocities and *Gaia* parallaxes and proper motions (Gaia Collaboration 2020) following the procedure described in Montes et al. (2001) and Maldonado et al. (2010). Briefly, the original algorithm (Johnson & Soderblom 1987) is adapted to epoch J2000 in the International Celestial Reference System (ICRS) as described in Sect. 1.5 of the HIPPARCOS and *Tycho* catalogues (ESA 1997). To take into account the possible correlation between the astrometric parameters, the full covariance matrix was used in computing the uncertainties. The corresponding (U, V) plane is shown in Fig. 2.

Most of our targets are in the region of the diagram occupied by the young stars (as expected); only some old stars taken from the literature (see above) are outside the boundary of this region. Once young stars were identified, we made use of Bayesian methods to confirm their membership to young stellar associations (BANYAN, Gagné et al. 2018)³.

³ <http://www.exoplanetes.umontreal.ca/banyan/banyansigma.php>

3.2. Rotational velocity

Rotational velocities were computed by means of the Fourier transform (FT) technique (e.g. Gray 2008). Briefly, the dominant term in the FT of the rotational profile is a first-order Bessel function that produces a series of relative minima at regularly spaced frequencies. The first zero of the FT is related to $v \sin i$ by

$$v \sin i = \frac{c}{\lambda} \times \frac{k_1}{\sigma_1}, \quad (1)$$

where c is the speed of light, λ is the central wavelength of the considered line, σ_1 is the position of the first zero of the FT, and k_1 is a function of the limb darkening coefficient (ϵ), which can be approximated by a fourth-order polynomial degree (Dravins et al. 1990):

$$k_1 = 0.610 + 0.062\epsilon + 0.027\epsilon^2 + 0.012\epsilon^3 + 0.004\epsilon^4, \quad (2)$$

where we assume $\epsilon = 0.6$ (see e.g. Gray 2008). Four spectral lines at 6335.33 Å, 6378.26 Å, 6380.75 Å, and 6393.61 Å were used for the computations. An additional line at 6400.11 Å was used but only for stars with high rotation values, because it is a blend of two lines that are resolved at low rotation levels. Given that it is not an isolated line, we only considered this blend if the derived $v \sin i$ value was compatible with the values obtained from the other lines.

In addition to the FT method, we fitted each line profile to a rotational profile following the prescriptions of Gray (2008). The fits were performed within a Bayesian framework based on a Monte Carlo Markov chain (MCMC) sampling of the parameter space. Since the rotational profile does not take into account the wings of the line profile (we note that the function is not defined on those points), the profile was convolved with a Lorentzian profile. Therefore, the model contains five parameters, namely the centre of the profile, the depth of the profile, the Lorentzian parameter, the amplitude of the profile, and an additional jitter term.

A comparison of the derived $v \sin i$ values obtained using the FT method and those derived using the line profile fitting is shown in Fig. 3 (left panel). Although the overall agreement is good, it can be seen that the line-profile-fitting method tends to provide slightly larger $v \sin i$ values. In particular, we note that for the Sun we obtain a mean value of $3.23 \pm 0.13 \text{ km s}^{-1}$ when using the FT method, and $4.43 \pm 0.26 \text{ km s}^{-1}$ from the profile-fitting technique (which can be compared with the adopted value of $\sim 2.0 \text{ km s}^{-1}$). Figure 3 also shows a comparison of our obtained equatorial velocities with those provided in the literature. The literature values are taken from the compilation of Glebocki & Gnacinski (2005, hereafter GL05). We see good agreement between our FT values and those from the literature overall (centre panel), especially at $v \sin i$ values larger than 10 km s^{-1} , with most stars lying close to the 1:1 relationship. However, the scatter is larger at lower rotation levels. The residual mean square (rms) of the comparison is 1.90 km s^{-1} , the root-mean squared error (rmse) is 3.6 km s^{-1} , and the R^2 (coefficient of determination) is ~ 0.98 . When considering the values derived from the line profile fitting (right panel), we obtain larger values than those found in the literature. This effect is more pronounced at the low rotation level. In this case, we obtain an rms value of 3.40 km s^{-1} , with an rmse value of 11.6 km s^{-1} , and $R^2 \sim 0.93$.

We conclude that the rotational-profile-fitting method works better at large rotational velocities. At low-rotation levels, the width of the line profiles are dominated by the intrinsic sources

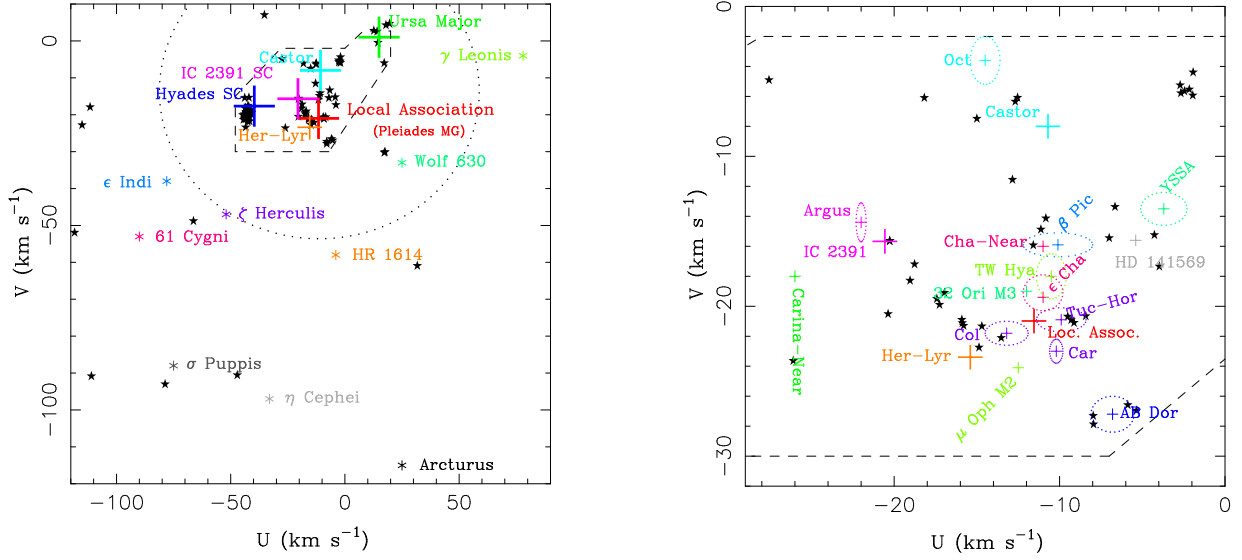


Fig. 2. (U, V) plane for the observed stars. *Left:* (U, V) plane showing the position of the known kinematic groups in the solar neighbourhood. Large crosses represent the convergence point of the ‘classical’ moving groups. Coloured asterisks show the positions of the so-called ‘old’ moving groups. Our stars are shown by black filled star symbols. The dashed line represents the boundary of the young disc population as defined by Eggen (1984, 1989). The dotted line represents the velocity ellipsoid determined by Francis & Anderson (2009). *Right:* zoom onto the region of the (U, V) plane around the Local Association.

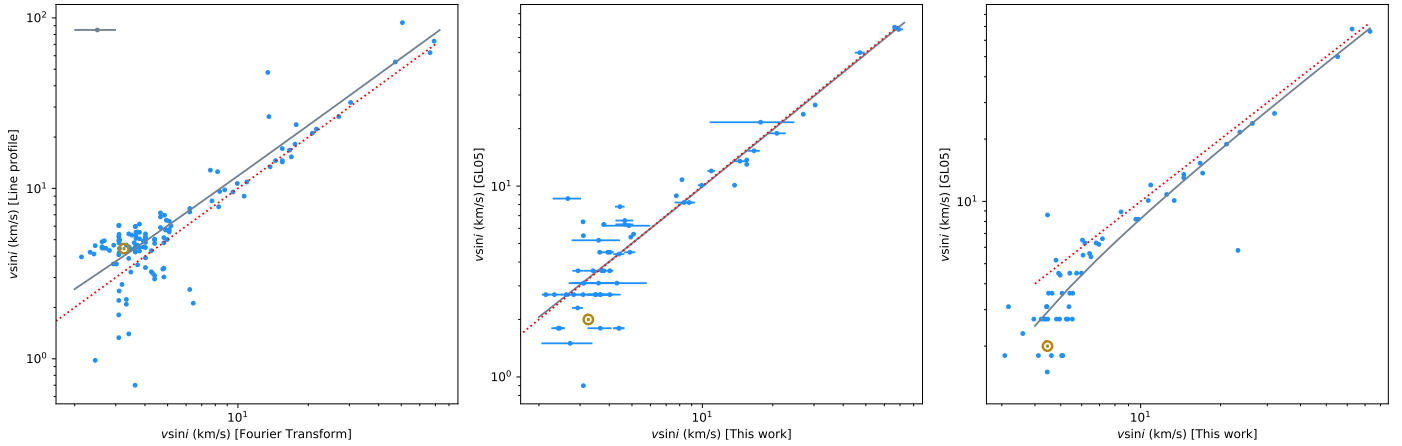


Fig. 3. *Left:* comparison between the $v \sin i$ derived from the fit of line profiles to a rotational profile, and $v \sin i$ derived using the FT technique. Centre: Comparison between the mean $v \sin i$ provided by GL05 and those measured in this work using the FT technique. *Right:* comparison between the mean $v \sin i$ provided by GL05 and those measured in this work by the fitting of line profiles to a rotational profile. The red dotted line shows the 1:1 relationship while the grey dashed line shows the best linear fit. The position of the Sun is shown with the symbol \odot . Typical error bars in GL05 data are of the order of 1.4 km s^{-1} .

of line broadening such as micro and macroturbulence, pressure, and magnetic Zeeman splitting. As a consequence, in slowly rotating stars, the fitting method tends to overestimate the $v \sin i$ values. Therefore, in the following, we consider only the $v \sin i$ values derived using the FT method.

3.3. Activity indexes

For the examination of activity indexes, we use the strong optical lines Ca II H and K, Balmer lines (from H α to H ϵ), Na I D₁, D₂, and He I D₃. Our definition of the bandpasses for the activity indexes follows Maldonado et al. (2019, and references therein). In order to transform the measured S index into R'_{HK} , a mean S index was computed for each star and transformed into the Mount Wilson scale by a comparison with the stars in common with Duncan et al. (1991). The comparison is shown in Fig. 4.

An ordinary least squares fit was performed in order to obtain a relationship between the S index measured in this work and the S index in the Mount Wilson scale. A 3σ clipping procedure was applied to identify outliers to the best linear fit. We note that the outliers correspond to stars for which only one measurement is available. Given their rather high S index values we speculate that these stars might have a high a level of chromospheric variability. We obtain the following relationship:

$$S_{\text{MW}} = (1.52 \pm 0.10) \times S_{\text{tw}} - (0.074 \pm 0.025), \quad (3)$$

where S_{MW} is the S index in the Mount Wilson scale and S_{tw} is the S index as measured in this work.

The S index contains the contribution from both the photosphere and the chromosphere. Empirical relationships to correct for the photospheric contribution were calibrated using the

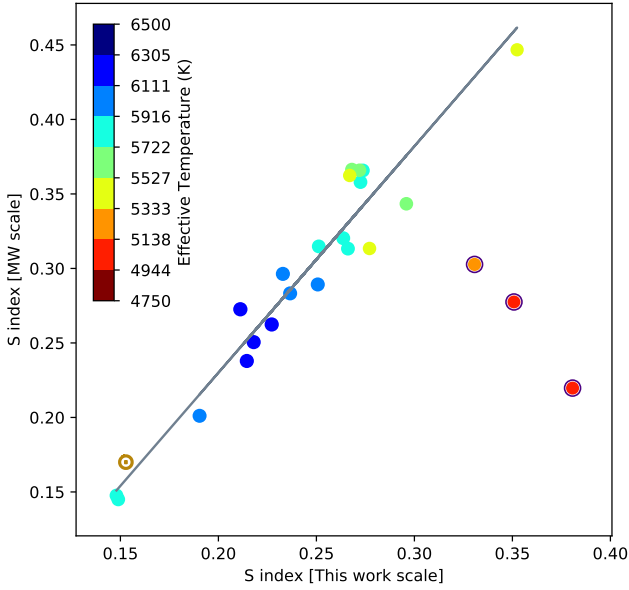


Fig. 4. Activity S index in the original Mount Wilson scale as a function of the S index as measured in this work. Different colours indicate the effective temperature of the stars. Outliers are highlighted by purple circles. Errors are within the symbol dimension. The best linear fit is shown in grey.

colour index ($B-V$). Furthermore, a conversion factor to correct for flux variations in the continuum passbands and normalise to the bolometric luminosity should be applied (Noyes et al. 1984). Unfortunately, there are no reliable B or V magnitudes available in the literature for most of our targets. Therefore, we used the *Gaia* DR2 (Gaia Collaboration 2018) effective temperature to estimate the ($B-V$) colour of our target stars. In order to do that, we derived a ($B-V$)– T_{eff} relationship using the data by Flower (1996). Details on this calibration are given in Appendix A.

The conversion factor and photospheric corrections most widely used are those provided by Noyes et al. (1984, hereafter NO84). However, they are only valid for solar-type stars with $0.44 < (B-V) < 0.82$ (spectral types between F5 and K2). More recently, Suárez Mascareño et al. (2015) derived conversion factors and photospheric corrections for cooler stars (up to $(B-V) = 1.9$).

3.4. Rotation periods and lifetime of active regions

In order to determine the stellar rotation period from the different activity indexes and the available TESS photometric time-series⁴, we started by using the Generalised Lomb–Scargle periodogram (Zechmeister & Kürster 2009) to identify periodic signals in the data. We then modelled the data using Gaussian Process regression in a Bayesian framework with the following likelihood:

$$\ln p(y_n, t_n, \sigma_n^2, \theta) = -\frac{1}{2} \mathbf{r}^T K^{-1} \mathbf{r} - \frac{1}{2} \ln \det K - \frac{N}{2} \ln 2\pi, \quad (4)$$

where y_n , t_n , σ_n are respectively the data, time of observations, and errors, θ is the array of parameters, \mathbf{r} is the residual vector

⁴ We use the two-minute cadence TESS light curves available for the systems. We use the data corrected for time-correlated instrumental signatures, thus the PDCSAP flux column in the FITS file (Jenkins et al. 2016).

obtained by removing the model from data, K is the covariance matrix, and N is the number of observations.

We selected the widely used quasi-periodic function obtained by multiplying a constant term to an exp-sin-squared kernel and to a squared-exponential kernel (george Python package, e.g. Ambikasaran et al. 2015; González-Álvarez et al. 2021; Maldonado et al. 2021), which is defined as follows:

$$k(i, j) = h^2 \exp \left(-\frac{(t_i - t_j)^2}{\tau^2} - \frac{\sin^2(\pi(t_i - t_j)/P_{\text{rot}})}{2\omega^2} \right), \quad (5)$$

where $k(i, j)$ is the i -th j th element of the covariance matrix, t_i and t_j are two times of the data set, h is the amplitude of the covariance, τ is the timescale of the exponential component, ω is the weight of the periodic component, and P_{rot} is the period.

We do not include an extra error term (σ_{jit}) as the uncertainties of the measured indexes are relative large. However, we added a linear trend model ($\gamma + \dot{\gamma}t$). At the beginning of the Gaussian Process regression, both data and errors were cleaned by a (3) sigma-clip procedure. The parameter space is sampled with emcee (Foreman-Mackey et al. 2013) set with 72 walkers randomly initialised within parameter boundaries; these are reported in Table 2. We imposed uniform priors on P_{rot} with boundaries according to the false alarm probability (FAP) of the maximum power GLS period. We used as prior boundaries $P_{\text{GLS}} \pm 1$ d, $P_{\text{GLS}} \pm 3$ d, $P_{\text{GLS}} \pm 8$ d, and $P_{\text{GLS}} \pm 15$ d for $\text{FAP} < 0.1\%$, $0.1\% < \text{FAP} < 1\%$, $10\% < \text{FAP} < 1\%$, and $10\% > \text{FAP}$, respectively. We note that for the analysis of the TESS photometric data, better results were obtained in some cases when using Gaussian priors centred around the known values of P_{rot} (see Sect. 5.4). Finally, we set a conservative burn-in phase of 40 K, while 10 K was used to obtain the posterior distributions.

4. The rotation–age–activity relationships

4.1. Rotation versus age and spectral type

Figure 5 shows the $v \sin i$ values as a function of the stellar age. The general tendency of lower rotation rates towards older stellar ages is clearly visible. We fit the data to a power law of the form:

$$v \sin i \propto \alpha \times t^\beta, \quad (6)$$

where the parameters α and β are drawn from a Bayesian framework using an MCMC simulation. The best-fit parameters are given in Table 3. The figure also reveals a dependency of the rotation versus age relationship on stellar spectral type. Rotation in cooler stars shows a lower decay than in hotter stars. In order to test this trend, we divided our target stars into three subsamples, namely stars hotter than 5790 K (i.e. G2-type stars), stars with effective temperatures of between 4800 K and 5790 K (spectral type between G2 and K2), and stars cooler than K2. The results are given in Table 3, and show that the β parameter (the slope) is greater for stars with spectral type earlier than G2, while the constant of proportionality, α , does not seem to vary according to the spectral type.

4.2. The stellar age–activity relationship

Figure 6 shows stellar age as a function of the level of stellar activity in terms of $\log R'_{\text{HK}}$. In order to allow comparison with previous works, we used the $\log R'_{\text{HK}}$ values derived using

Table 2. Model priors.

Parameter	Priors	Description
<i>linear trend</i>		
γ	$\mathcal{U}(\min(\text{index}), \max(\text{index}))$	Minimum and maximum value of the index
$\dot{\gamma}$	$\mathcal{U}(\min(\text{slope}), \max(\text{slope}))$	Slopes of the data computed in the first and second half-seasons of the observations (d^{-1})
<i>GP parameters</i>		
h	$\mathcal{LU}(10^{-6}, 10^{+6})$	
τ	$\mathcal{LU}((\text{minimum } P_{\text{rot}} \text{ prior})/2, 10^4)$	(d)
ω	$\mathcal{LU}(10^{-2}, 10)$	
P_{rot}	$\mathcal{LU}(P_{\text{GLS}} \pm nm \text{ d})$	nm depends on the FAP, see text (d)

Notes. Labels \mathcal{U} and \mathcal{LU} represent uniform and log-uniform distribution, respectively, while P_{GLS} is the period of maximum power obtained from the GLS periodogram.

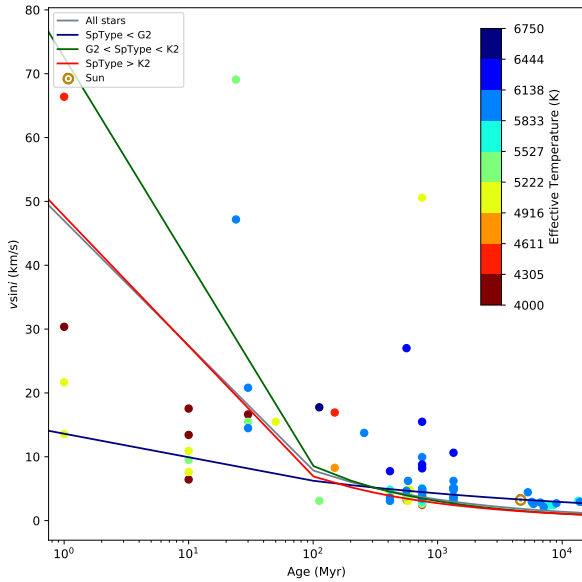


Fig. 5. Projected rotational velocity, $v \sin i$, as a function of stellar age. Different colours indicate the effective temperatures of the stars. Solid lines indicate the best fit.

Table 3. Best derived parameters for the fit $v \sin i = \alpha \times t^\beta$.

Sample	α	β	N
All stars	$44.34^{+0.07}_{-0.07}$	$-0.3760^{+0.0003}_{-0.0003}$	127
SpType < G2	$13.41^{+0.15}_{-0.15}$	$-0.166^{+0.002}_{-0.002}$	45
G2 < SpType < K2	$67.29^{+0.20}_{-0.20}$	$-0.4478^{+0.0005}_{-0.0005}$	64
SpType > K2	$44.74^{+0.08}_{-0.09}$	$-0.4051^{+0.0005}_{-0.0005}$	18

the NO84 prescriptions. The dotted line shows the empirical relationship obtained by MH08.

It can be seen that the MH08 relationship predicts slightly younger ages for stars older than the Hyades. However, our sample is affected by several biases. To start with, only 23.3% of our stars are younger than ~ 500 Myr (and only one has a colour index within the range of the NO84 calibrations). Another bias that might affect our results is the fact that, at older ages, our sample is mainly composed of stars with effective temperatures

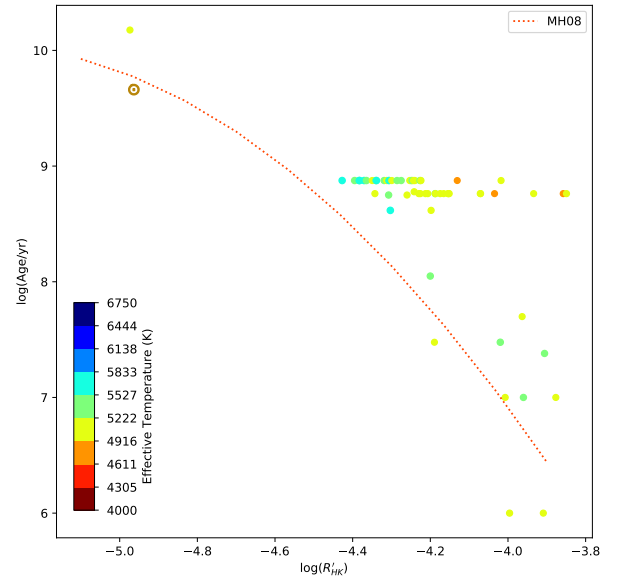


Fig. 6. Stellar age as a function of $\log R'_{\text{HK}}$. Different colours indicate the effective temperatures of the stars. The dotted line shows the relationship obtained by MH08. The position of the Sun is shown with the symbol of a dot inside a circle \odot .

of greater than ~ 5500 K, and therefore they show lower levels of stellar activity than otherwise similar cooler stars. The dependency of the age–activity relationship on spectral type is quite clear when looking at the stars in the Hyades cluster, where it can be seen that cooler stars show higher levels of activity.

4.3. Flux–flux relationships

Emission excesses in the Ca II H and K and H α lines were determined using the spectral subtraction technique (e.g. Montes et al. 1995, 2000). Briefly, the basal chromospheric flux is removed using the spectrum of a non-active star of similar stellar parameters and chemical composition to the target star as reference.

Reference stars were selected from Martínez-Arnáiz et al. (2010). Fluxes were derived from the measured equivalent width in the subtracted spectra by correcting the continuum flux:

$$\log(F_\lambda) = \log(EW) + \log(F_\lambda^{\text{cont}}), \quad (7)$$

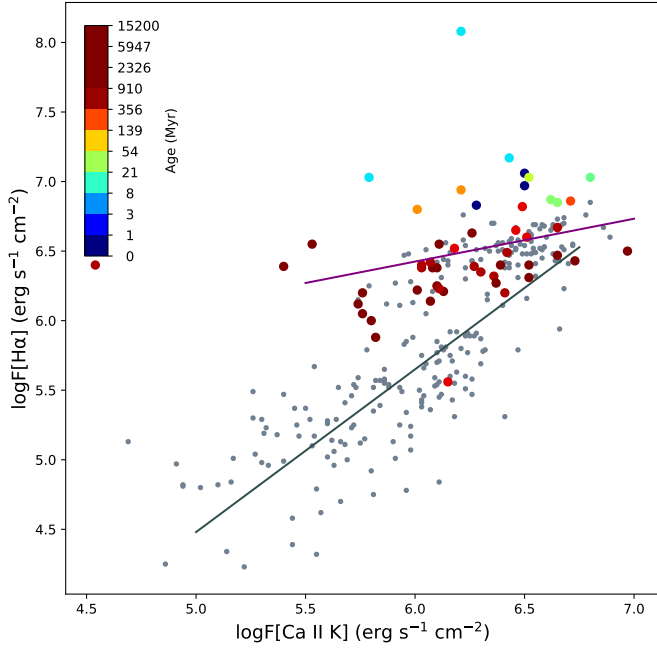


Fig. 7. Flux–flux relationship between H α and Ca II K. Different colours indicate the ages of the stars. For comparison, data for FGKM stars from the literature (López-Santiago et al. 2010; Martínez-Arnáiz et al. 2010) are also plotted as grey circles. Our best linear fit for the upper branch is shown with a purple line, while the grey line shows the fit for the lower branch derived by Martínez-Arnáiz et al. (2011b).

where the continuum flux, $F_{\lambda}^{\text{cont}}$, was determined using the empirical calibrations with the colour index, $(B-V)$, derived by Hall (1996).

Figure 7 shows the comparison between the flux in the H α line and the flux in the Ca II K line. A fit to a power-law function provides

$$\log(F_{H\alpha}) = (4.58 \pm 0.67) + (0.31 \pm 0.11) \times \log(F_{CaK}). \quad (8)$$

Martínez-Arnáiz et al. (2011a,b) identified two branches in the H α versus Ca II K flux–flux relationship. The lower or inactive branch has a slope of 1.17 ± 0.08 and is composed of field stars. On the other hand, the upper or active branch is composed of young late-K and M stars and has a slope of 0.53 ± 0.08 . Our sample provides a slope of 0.33 for the active branch showing that young F-G stars share the behaviour of cooler young stars. However, we note that for most of our inactive stars we were not able to measure any emission excess, and so we were only able to identify one star (namely HD 167389) in the inactive branch. Figure 7 also shows that there seems to be a tendency of higher H α fluxes for the youngest stars, which show a rather flat H α versus Ca II K relationship. We note that the different importance of H α and Ca II emission might suggest that the different types of active structures have different roles (see Meunier & Delfosse 2009, for the case of the Sun). It should also be noted that formation of the H α line is much more subject to non-local thermodynamic equilibrium effects than the Ca II lines as well as to further complications in cool stars (this is because unlike the Ca II H and K lines, the H α line is not a resonance transition). The star TYC 6779-305-1 shows very strong emission in the H α line and departs from the other young stars in the flux–flux relationship.

5. Temporal evolution of active regions

5.1. Pooled variance analysis

We apply the pooled variance (PV) technique (see e.g. Donahue et al. 1997a,b; Messina & Guinan 2003; Lanza et al. 2004; Scandariato et al. 2017) to the time-series of the Ca II H and K activity index. Briefly, the data are binned into time intervals of length t_{pool} . Then, first the variance is calculated for each bin, and then the average of these variance values is computed forming the so-called pooled variance. This is done for a range of t_{pool} values across the duration of the monitoring observations. The characteristic timescales of the star are shown by the position where the PV versus t_{pool} changes behaviour.

Before applying the PV method to our stars we performed a series of simulations in order to understand the performance of the method as well as the effect of the sampling on the derivation of rotation periods and AR lifetimes. In our first test, we took advantage of the solar spectra taken by the HARPS-N solar telescope and used the three years of S index values published in Maldonado et al. (2019). We computed the PV diagram using the original dataset and compared it with the PV diagram obtained by sampling the data using the observation times of three selected stars. The corresponding plot is shown in Fig. 8 (top left). Specifically, ‘sampling 1’ contains 83 data points covering a time-span of ~ 1.5 yr. The data are divided into two main observing seasons with a gap of ~ 200 d between them. ‘Sampling 2’ is composed of 41 observation points taken in 1.3 yr. As in ‘sampling 1’ there is a gap of 200 d between the two main observing seasons, but the second season is less populated than the first one. Finally, in ‘Sampling 3’ we consider only 22 data points, covering ~ 200 d, with a gap of ~ 100 d between the two main observing seasons. The temporal coverage of the different samplings can be seen in the inset of the figure. The results show that, even with the most infrequent sampling (case 3, in purple), we are able to recover the rotation period with a value in the range 20–30 d. However, the AR lifetime is only recovered when using the original time-series (in red), with a value between 200 and 300 d.

As the Sun is clearly not representative of most of our young stars, we performed three additional simulations. In simulation 1 (Fig. 8, top right), we consider a short rotation period of 2.74 d and an AR lifetime of 10 rotation periods. In simulation 2 (Fig. 8, bottom left), we keep the rotation period at 2.74 d but consider an AR lifetime of four rotation periods. Finally, in simulation 3 (Fig. 8, bottom right), we fix the rotation period at 9.4 d, and the AR lifetime to four rotation periods. The simulations were performed while considering a sinusoidal behaviour, modulated with an exponential decay. In order to simulate the effect of spot growth and decay, as the time runs and the amplitude of the variability decays, another sinusoidal signal (with the same period but a different phase) is included.

It can be seen that in the short-period cases, we are not able to recover the injected rotation period (even with the original dataset), as the PV steadily increases until the AR lifetime is reached. However, the AR lifetime seems well constrained even for samplings 1 and 2. In the case of sampling 3, without any priory knowledge of the AR lifetime, we would have concluded that the PV diagram is too complex to derive any meaningful conclusion. Finally, for simulation 3, we are able to recover the AR lifetime in all cases. The injected rotation period is also recovered, although at a slightly shorter value, ~ 7 –8 d.

These simulations show that, with the data at hand, short rotation periods as well as long AR lifetimes may be difficult

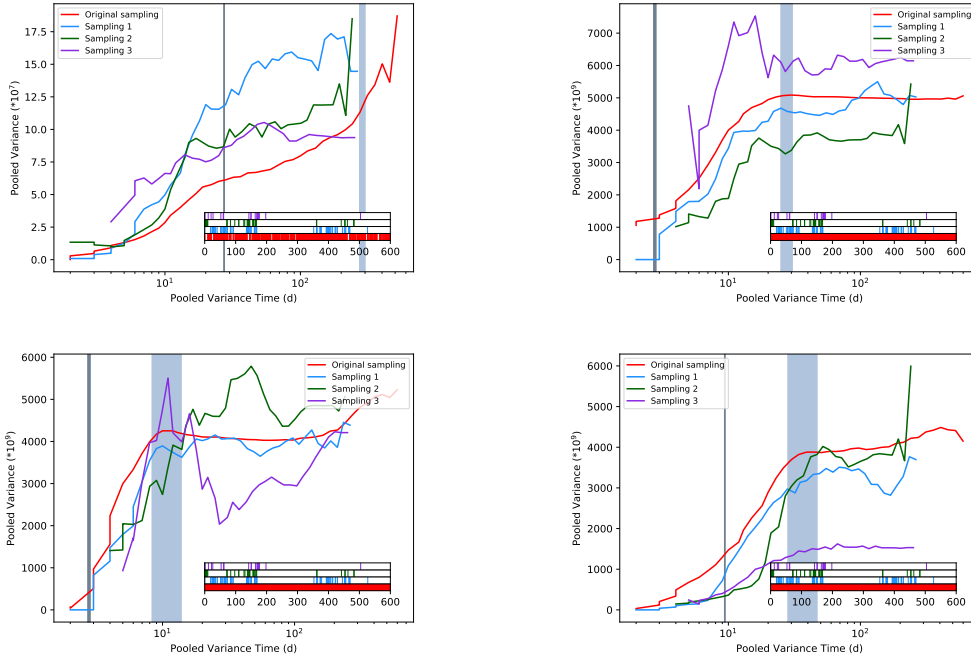


Fig. 8. Pooled variance profile for the HARPS-N Solar S -index (*up left*), and simulated S -index time-series for different temporal samplings. The plot shows a smoothed function of the PV to improve the readability of the plots. The vertical lines show the simulated rotation periods and AR lifetimes. The inset plots show the temporal coverage of the different samplings.

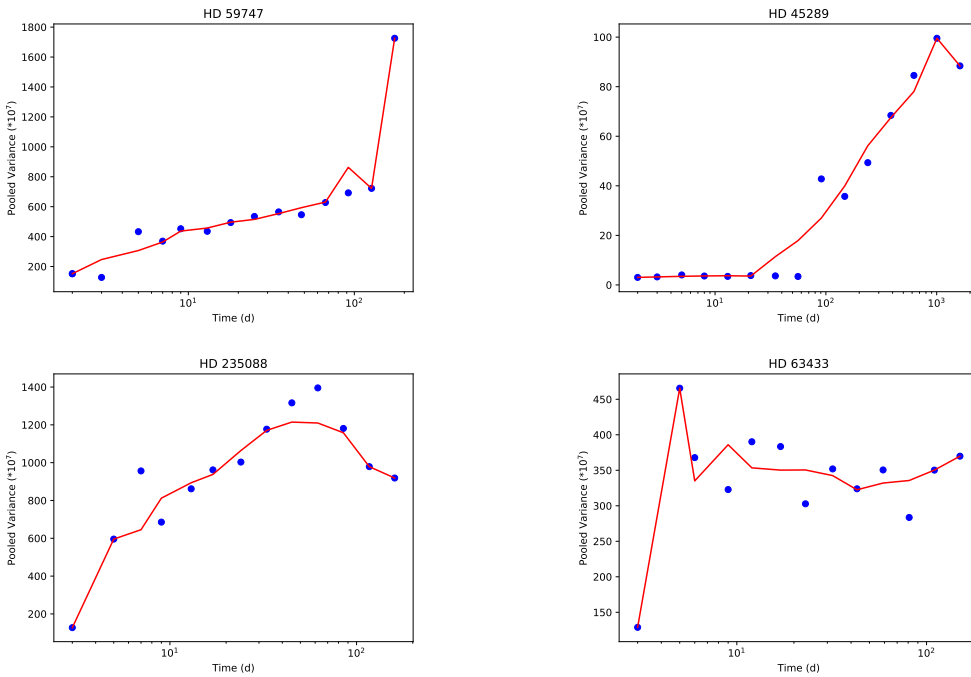


Fig. 9. Pooled variance profile for HD 59747 (*up left*), HD 45289 (*up right*), HD 235088 (*bottom left*), and HD 63433 (*bottom right*). The red line is a smoothed function that highlights the trend of the data for ease in reading of the plots.

to identify with the PV technique. Therefore, we set a limit of at least 20 observations per star to use the method.

Figure 9 (up left) shows an example of a star (HD 59747) with a well-defined pattern. It can be seen that, for this star, the PV steadily increases up to a t_{pool} value of ~ 8 d and then shows a plateau where the PV remains roughly constant. The PV starts to increase again at $t_{\text{pool}} \sim 70$ – 100 d. We conclude that the rotation period of this star is around 8 d, and that active regions have typical evolution timescales of approximately ten rotation periods. We note that these estimates are in agreement with the results from the GLS and GP analysis.

Other stars like HD 45829 (Fig. 9, up right) show a different profile. In this case, the PV shows a small roughly constant value at small t_{pool} values. However, after ~ 20 – 30 d, the PV shows a nearly constant increase of variance with increasing

timescale. These stars are dominated by non-periodic variations with substantial active-region evolution masking the rotational plateau.

In stars like HD 235088 (Fig. 9, bottom left), the rotational plateau is not found and the PV increases until the active-region evolution timescale is reached at ~ 200 d. Other stars show high PV on short timescales, which then diminishes. For example, HD 63433 (Fig. 9, bottom right) shows a peak at ~ 7 d (in agreement with its rotation period) and then the PV steadily decreases (this could be due to statistical fluctuations attributable to a rather small number of data points in this interval of time or the presence of outliers) until it remains constant. Finally, some stars have rather complex patterns (e.g. TAP 26), the PV shows a large scatter, and their temporal variation is not well-defined, while stars like HIP 21112 show roughly constant patterns.

Figure B.1 shows the PV diagram for all stars with more than 20 observations.

5.2. Active-region lifetimes from light-curve analysis

Once we had explored the behaviour of our sample in terms of the activity–age and flux–flux relationships, as well as in the pooled variance diagrams, we made use of available TESS photometry to study whether the inferred lifetimes of ARs show any dependency on stellar properties, particularly stellar age. Several recent works made use of light curves to infer the properties of active regions. The idea behind these methods is that the decay time of the autocorrelation function (ACF) is known to be related to the characteristic decay time of starspots (Lanza et al. 2014). In particular, Giles et al. (2017, hereafter GI17) modelled the ACF of light curves using an underdamped harmonic oscillator with an interpulse term. However, Santos et al. (2021, hereafter SA21) discussed this choice of the modelling function, and suggested a new modelling with a linear decay. On the other hand, Basri et al. (2022, hereafter BA21) uses a method based on the strengths of the first few normalised autocorrelation peaks.

In order to test whether or not these methods can be suitable for our stars, we start by computing the ACF of the TESS light curves. We note that the ACF can be calculated only for stars for which the data have a continuous sampling (or at least that can be interpolated to a continuous sampling). Otherwise, the strength of the ACF peaks might show a complicated dependency on the spectral window. The corresponding ACF curves are shown in Fig. B.2, while the properties of the ACF analysis are given in Table 4.

Inspection of the figure reveals that, for some stars, the peaks of the ACF always have the same strength (e.g. V830 Tau, TAP 26). This means that the active regions should be stable during the time-span of the observations. In addition, there seems to be no beating in these curves, which is usually due to differential rotation. As the ACFs of these stars show no sign of time-decay, it is unlikely that the methods presented in GI17, SA21, or BA21 will work. Indeed, when we try to fit the ACF curve of these stars to one of the functional forms described in GI17 or SA21, the result is that the posterior distribution of the AR lifetime is not well constrained, but is shifted towards the larger prior of the AR lifetime. We illustrate this in the left panel of Fig. B.3, where we show the posterior distribution for the case of the star V830 Tau. It is clear that while all parameters are well constrained, the fit is not able to derive any meaningful AR lifetimes. We classify these curves as ‘sin’ (sinusoidal) or ‘per’ (periodic) to indicate that there is no time-decay present in the ACF curve. With the data at hand, the only information that we can extract for these stars is that the typical AR lifetime should be much longer than the time-span of the observations.

Other stars, such as HIP 92680 and HIP 105388, show a clear time-decay. For these stars, we used a Bayesian framework to model the ACF curve to the functional forms described in GI17 (exponential decay) and SA21 (linear decay). As an example, we show the posterior distribution of the fit for the case of HIP 105388 (Fig. B.3, right). We used the Bayesian inference criterion (BIC) as a measure of the goodness of the two models, although in most cases the BICs of the two models are almost identical (i.e. there is no significant evidence that one model is ‘better’ than the other). We note that for some stars, even if the posterior distribution of all the fitted parameters are well constrained, the best fit is not able to reproduce all the features seen in the ACF (e.g. V1090 Tau or V1298 Tau). This might indicate that these ACFs are not fully regular. Indeed, some of our stars

Table 4. Summary of the ACF analysis of the TESS light curves.

Star	ACF-fit τ (d)	ACF-type	ACF-fit form
HIP 490	$232.59^{+474.93}_{-106.83}$	sin + decay	exp
HIP 1481		sin + decay	bad fit
TYC 4500-1478-1	$132.92^{+248.64}_{-52.46}$	sin + decay	exp
V1090 Tau	$135.47^{+407.07}_{-66.71}$	sin + decay	exp ^(†)
V1298 Tau	$259.36^{+687.93}_{-155.05}$	per + decay	lin ^(†)
HD 285507		other	
HIP 19859	>>26	per	
TAP 26	>>24	per	
HD 285773	>>25	per	
V1202 Tau	>>24	sin	
HIP 21112	>>26	sin	
V830 Tau	>>24	sin	
TYC 5909-319-1	$387.19^{+761.66}_{-238.44}$	sin + decay?	exp ^(†)
HD 32923		other	
HD 36108		other	
HD 38283	$42.19^{+89.43}_{-15.72}$	per	exp ^(†)
HIP 27072		other	
HD 45289		other	
HD 59747	>>27	sin	
HD 63433	$62.31^{+37.82}_{-14.29}$	sin + decay	lin ^(†)
HD 70573	>>25	sin	
TYC 1989-0049-1		other	
HD 107877		other	
BD+26 2342	$64.07^{+55.15}_{-18.58}$	sin + decay?	exp
BD+27 2139	>>27	sin	
HIP 61205		other	
HD 122862		other	
HD 167389		other	bad fit
HIP 92680	$232.93^{+714.18}_{-155.27}$	per + decay	lin
HD 235088		other	
HD 191408		other	
HD 196378		other	
HIP 105388	$82.95^{+33.26}_{-18.16}$	per + decay	exp

Notes. ‘sin’: the ACF is clearly sinusoidal without an apparent time-decay; ‘per’: the ACF is periodic without an apparent time-decay; ‘decay’: a time-decay is seen in the ACF; ‘other’: the ACF does not fit in the other categories; ‘exp’: fit to an exponential decay following GI17; ‘lin’: fit to a linear decay following SA21; ^(†)the best fit does not properly model the curve.

show a rather irregular ACF curve that makes its analysis difficult. Some examples are HD 28557 and or HD 32923. Table 4 provides the AR lifetimes or lower limits derived from the ACF curves, when possible.

5.3. Active-region lifetime as a function of stellar parameters

The top panel of Fig. 10 shows the timescale of AR evolution derived from the ACF analysis of the TESS light curves as a function of stellar age. Given the uncertainties involved in age and AR lifetime and that the number of points is rather low, any conclusion from this figure should be taken with caution. Nevertheless, the figure reveals a tendency of younger stars to show longer AR lifetimes. The Spearman’s rank test, ρ , is -0.67 with a p-value of 0.03 (the lower limits on AR lifetimes were not considered).

We also checked for correlations between AR lifetimes, the effective temperature of the star (Fig. 10, top right), and the level

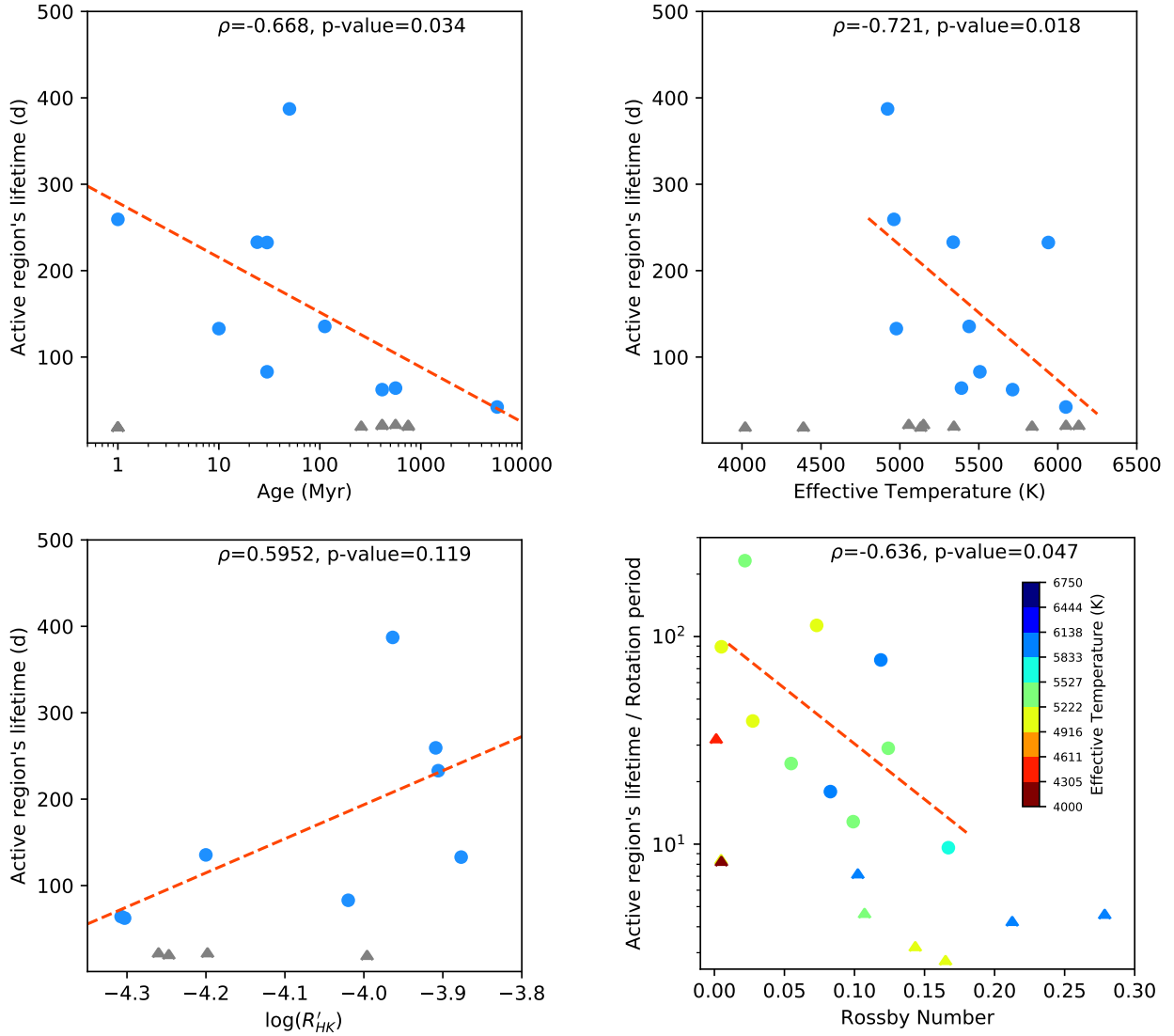


Fig. 10. Timescale of AR evolution derived from the ACF analysis of the TESS light curves as a function of stellar age (*top left*), effective temperature (*top right*), $\log R'_{\text{HK}}$ value (*bottom left*), and Rossby number (*bottom right*). Stars with lower limits on the AR timescale are shown with triangles. A linear fit (dashed orange-red line) is shown to guide the eye.

of activity (as measured by the $\log R'_{\text{HK}}$ value); see bottom left panel of Fig. 10. A general tendency of increasing AR lifetime with cooler temperatures and higher activity levels seems to be present in the data. Whilst the AR lifetime correlation with T_{eff} appears to be statistically significant (with a p -value lower than 0.02), the correlation between AR lifetime and activity level does not (p -value ~ 0.12). These results are in agreement with the findings of GI17, SA21, and BA22 who analysed a large dataset of KEPLER light curves and concluded that ARs decay more slowly in cooler stars.

It is worth noting that when comparing stars with different stellar parameters, other properties like the convective turnover time might be different as well. The use of the Rossby number has been shown to substantially improve the observed activity–rotation relations for main sequence, solar-type stars (e.g. Noyes et al. 1984). To compute the Rossby number, we first estimate the mass of our stars using the *Gaia* DR2 luminosities (Gaia Collaboration 2018) and the mass–luminosity relationship provided by Wang & Zhong (2018). We then derive the convective turnover timescales by interpolating (in stellar mass and age) the theoretical tracks provided by Spada et al. (2013).

Figure 11 shows the position of our target stars in the stellar mass–age diagram where it can be seen that most of our targets have masses in the $0.8\text{--}1.1 M_{\odot}$ range. Finally, the Rossby number is computed as

$$R_0 = \frac{P_{\text{rot}}}{\tau_{\text{conv}}}. \quad (9)$$

The bottom right panel of Fig. 10 shows the timescale of AR evolution as a function of the Rossby number. For a better comparison between stars with different properties, we show the AR lifetime in units of the corresponding rotational period. The figure shows a clear tendency of decreasing AR lifetimes with increasing Rossby number, which would imply that ARs survive longer in stars with larger convective turnover timescales and shorter rotation period. A Spearman’s correlation test returns the values $\rho = -0.64$ and $p\text{-value} = 0.05$.

5.4. Gaussian process analysis of the spectroscopic indexes

In this section we explore whether or not our spectroscopic time-series can be used to infer the AR lifetimes. This would be of

Table 5. Rotational periods derived from TESS, ASAS, SWAPS, PV analysis, and the literature.

Star	TESS (d)	ASAS (d)	SWAPS (d)	Other (d)	Pooled Variance (d)
HIP 490	3.01				
HIP 1481	2.41				~3
TYC 4500-1478-1 ^(†)	3.39	3.42		3.5 (STELLA)	~6
V1090 Tau ^(†)	4.68	4.76	4.71		
V1298 Tau ^(†)	2.91		2.89/1.44	2.91 (Suárez Mascareño et al. 2021)	
HD 285507	5.76	10.57		2.24 (Carleo et al. 2020)	
HIP 19859	5.85				
TAP 26 ^(†)	0.71	0.71		0.71 (Grankin 2013)	
HD 285773	5.14	1.9/4.6		10.7? (Douglas et al. 2019)	~6
V1202 Tau ^(†)	2.72	2.7	1.59	2.68 (STELLA)	
HIP 21112	5.40				
V830 Tau ^(†)	2.77	2.74	1.37	2.74 (Damasso et al. 2020)	
TYC 5909-319-1 ^(†)	3.42	3.37	1.41/3.4	3.43 (Carleo et al. 2021)	
HD 32923	3.43			32 (Schmitt & Mittag 2020)	~3/4
HD 36108	2.48		2.99?		~2/3
HD 38283	2.36				
HIP 27072 ^(†)	6.21			5.9 (Montesinos et al. 2016)	
HD 45289	4.37				
HD 59747 ^(†)	8.04				~8
HD 63433 ^(†)	6.48		7.98	6.45 (Mann et al. 2020)	~4/5?
HD 70573 ^(†)	3.32			3.28 (STELLA)	
TYC 1989-0049-1	12.16	8.27	10.86	5.5/11 (STELLA)	
HD 107877	9.25			7.3?/1.16? (STELLA)	
BD+26 2342 ^(†)	4.99			4.6 (GAPS data)	
BD+27 2139 ^(†)	9.37		9.29	9.28 (STELLA)	~4/5?
HIP 61205	5.91		7.58	7.39 (STELLA)	
HD 122862	3.80				~3
HD 167389 ^(†)	7.70			8.85 (GAPS data)	~7/8
HIP 92680	1.00				
HD 235088	6.14			14.1 (REM), 12.8-13.5 (STELLA)	
HD 191408	3.44				
HD 196378	8.86				
HIP 105388	3.39				

Notes. ^(†)Star selected for the detailed comparison of the different activity indexes. They are shown in Figs. 13 and 14.

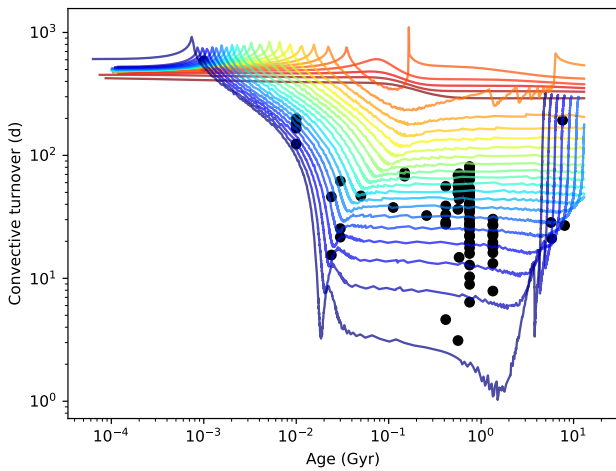


Fig. 11. Convective turnover timescale as a function of stellar age. The black circles show the stars studied in this work while the continuous lines represent the tracks provided by Spada et al. (2013). The models have solar metallicities and stellar masses ranging from $0.10 M_{\odot}$ to $1.25 M_{\odot}$ (from red to violet) with a mass step of $0.05 M_{\odot}$.

utmost interest as it would provide a complementary approach to the use of light curve ACFs. Through this analysis, we use the results of the GP analysis (see Sect. 3.4) and make the assumption that the GP hyperparameter τ (i.e. the timescale of the exponential decay; see Eq. (5)) corresponds to the AR growth and decay lifetime. Whether or not this assumption is well founded is discussed below.

For this analysis, we focus only on stars with more than 20 observations and with available TESS photometry. As most of our targets are young, they should have short rotation periods and therefore the rotation periods derived from the TESS data should be reliable. We note that the GP analysis has already been used in the literature to derive rotation periods (e.g. Angus et al. 2018). However, given that the rotation period is a key parameter of the analysis, we performed a comparison with other photometric surveys like ASAS (Shappee et al. 2014; Jayasinghe et al. 2019), SWAPS (Butters et al. 2010), STELLA (Strassmeier et al. 2004), and other literature sources. Table 5 provides a summary of the derived rotation periods. The TESS rotation periods are derived from our GP analysis.

In addition, the TESS-derived periods can be translated into equatorial velocities, v_{eq} , and compared with the corresponding

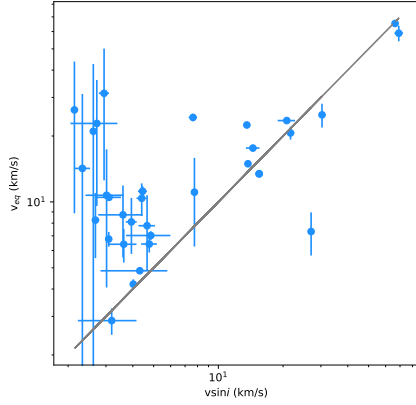


Fig. 12. Equatorial velocities (derived from the TESS P_{rot} and R_{\star}) versus projected rotational velocities, $v \sin i$.

$v \sin i$ values. In order to perform this conversion, stellar radii are taken from *Gaia* DR2 (Gaia Collaboration 2018). The corresponding plot is shown in Fig. 12. As expected, most of the targets lie in the region v_{eq} larger than $v \sin i$, while 14 stars are close to the line $v_{\text{eq}} \sim v \sin i$ and should have inclination angles ~ 90 degrees. We note that one star, namely HD 107877, has a P_{rot} value that translates into non-physical v_{eq} values (i.e. shorter than $v \sin i$). For this star, no clear P_{rot} was found in the analysis of the ASAS or SWAPS photometry, while the STELLA data show two peaks at ~ 7.3 d and ~ 1.6 d. We note that the 7.3 d signal is still too large to be compatible with the $v \sin i$ value.

In the following, we retain for study only those stars for which: the number of spectroscopic observations is larger than 20, TESS photometry is available, and we have independent confirmation from at least one other study that the TESS-derived period is correct. These stars are highlighted in Table 5.

Figure 13 shows the rotation periods derived from the GP analysis of the Ca II, the Balmer lines, He I D₃, and Na I D₁, D₂ activity indexes as a function of the reference TESS-derived rotation periods. The corresponding comparison for the derived AR lifetimes is shown in Fig. 14.

We note that for most of the stars, the rotation periods derived from the spectroscopic indexes are significantly shorter than the TESS-derived periods. For example, for BD+27 2139 (which has a TESS-derived period of 9.37 d) the analysis of the different spectroscopic indexes provides values in the range ~ 2 – 3 d. On the other hand, AR lifetimes derived from spectroscopic indexes are much longer than those derived from the TESS data.

Furthermore, even if the periods from different indexes agree, AR lifetimes can be very different from one index to another. An example is the star V830 Tau, for which we recover a rotation period of ~ 2.77 d in TESS, Ca II, H δ , and H ϵ data. However, the AR lifetime varies from ~ 5.32 d in the TESS data to ~ 2970 d in the Ca II H and K data (we note that for this star, from the ACF light curve analysis we only conclude that its AR lifetime should be longer than 24 d.)

We conclude that the GP analysis of the spectroscopic indexes does not allow us to measure AR lifetimes with sufficient accuracy. Several explanations can be put forward to account for this result. The first one refers to the data and the assumptions used in this work. We note that the bulk of the stars analysed here come from a radial-velocity exoplanet program, and therefore the number of observations, temporal baseline, and sampling vary considerably from one star to another and in some cases may not be optimal. We highlight the fact that only stars in which potential planetary signals are identified are observed with a high cadence. Furthermore, it is important to keep in mind that GPs

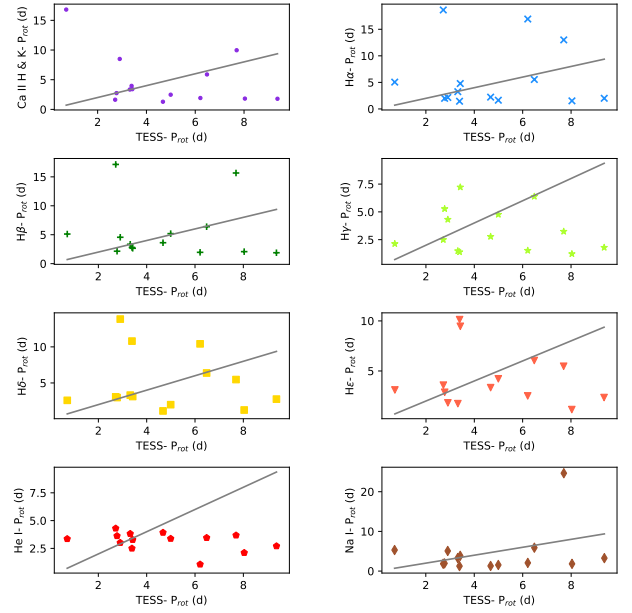


Fig. 13. Derived rotation periods from the GP analysis of the different spectroscopic indexes as a function of the values derived from the GP analysis of the TESS photometry.

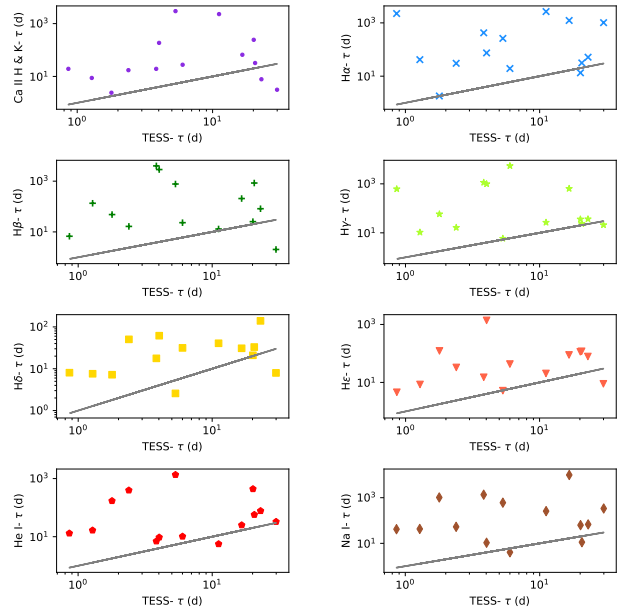


Fig. 14. Derived AR lifetimes from the GP analysis of the different spectroscopic indexes as a function of the values derived from the GP analysis of the TESS photometry.

are simplified ad hoc models of stellar activity and that the correspondence between the GP hyperparameters and the physical properties of AR should be further analysed.

6. Conclusions

In this work, a detailed analysis of a large sample of young stars with well-known derived ages determined from their membership to kinematic associations and moving groups is performed. Projected rotational velocities and activity indexes are determined in a homogeneous way from high-resolution optical spectra. The temporal series of the different activity indexes are used together with a Gaussian process regression analysis to infer rotational periods and the lifetime of AR growth and decay.

We characterise our sample in terms of activity–rotation–age and flux–flux relationships and confirm the well-known trend of decreasing activity and rotation with stellar age. We also show that cooler stars show higher levels of activity and that their rotation rate shows a lower age-decay than their hotter counterparts. We also find that young F and G stars depart from the inactive stars in the flux–flux relationships.

We searched for correlations between the ARs evolution lifetime and the stellar properties, namely age, effective temperature, and activity level. AR lifetimes derived from the ACF analysis of light curves show a tendency to decrease with stellar age. AR lifetimes are also found to be lower in hotter and inactive stars. A global tendency of larger AR lifetimes versus lower Rossby number is also found. However, we caution that these relationships are affected by the low number of stars for which a reliable AR lifetime could be obtained. Finally, one cannot forget the assumptions linked to the models used to determine stellar ages or the convective turnover timescale. We also tried to derive AR lifetimes from a GP modelling of the spectroscopic time-series but the results were largely unsatisfactory, even though we restricted the analysis to stars with well-known rotation periods from photometric data.

Further observations of stars covering a wide range of stellar ages, together with a better understanding of how to model stellar activity, as well as an accurate determination of the stellar properties will help us to understand whether ARs have rather irregular lifetimes or if there is some unknown relationship between AR lifetime and stellar properties.

Acknowledgements. J.M., S.C., A.P., G.M. acknowledge support from the Accordo Attuativo ASI-INAF no. 2021-5-HH.0, Partecipazione alla fase B2/C della missione Ariel (ref. G. Micela). S.C. acknowledge financial contribution from the agreement ASI-INAF no. 2018-16-HH.0 (THE StellaR PAtH project). We sincerely appreciate the careful reading of the manuscript and the constructive comments of the referee Gibor Basri.

References

- Agüeros, M. A., Bowsher, E. C., Bochanski, J. J., et al. 2018, *ApJ*, **862**, 33
- Ambikasaran, S., Foreman-Mackey, D., Greengard, L., Hogg, D. W., & O’Neil, M. 2015, *IEEE Trans. Pattern Anal. Mach. Intell.*, **38**, 252
- Angus, R., Morton, T., Aigrain, S., Foreman-Mackey, D., & Rajpaul, V. 2018, *MNRAS*, **474**, 2094
- Baker, J., Bizzarro, M., Wittig, N., Connelly, J., & Haack, H. 2005, *Nature*, **436**, 1127
- Barnes, S. A. 2007, *ApJ*, **669**, 1167
- Barrado y Navascues, D. 1998, *A&A*, **339**, 831
- Basri, G., Streichenberger, T., McWard, C., et al. 2022, *ApJ*, **924**, 31
- Bell, C. P. M., Mamajek, E. E., & Naylor, T. 2015, *MNRAS*, **454**, 593
- Brandt, T. D., & Huang, C. X. 2015, *ApJ*, **807**, 58
- Butters, O. W., West, R. G., Anderson, D. R., et al. 2010, *A&A*, **520**, L10
- Carleo, I., Malavolta, L., Lanza, A. F., et al. 2020, *A&A*, **638**, A5
- Carleo, I., Desidera, S., Nardiello, D., et al. 2021, *A&A*, **645**, A71
- Cosentino, R., Lovis, C., Pepe, F., et al. 2012, *SPIE Conf. Ser.*, **8446**, 84461V
- Covino, E., Esposito, M., Barbieri, M., et al. 2013, *A&A*, **554**, A28
- Dahm, S. E. 2015, *ApJ*, **813**, 108
- Damasso, M., Lanza, A. F., Benatti, S., et al. 2020, *A&A*, **642**, A133
- Delorme, P., Collier Cameron, A., Hebb, L., et al. 2011, *MNRAS*, **413**, 2218
- Donahue, R. A., Dobson, A. K., & Baliunas, S. L. 1997a, *Sol. Phys.*, **171**, 191
- Donahue, R. A., Dobson, A. K., & Baliunas, S. L. 1997b, *Sol. Phys.*, **171**, 211
- Douglas, S. T., Curtis, J. L., Agüeros, M. A., et al. 2019, *ApJ*, **879**, 100
- Dravins, D., Lindegren, L., & Torkelsson, U. 1990, *A&A*, **237**, 137
- Dumusque, X., Cretignier, M., Sosnowska, D., et al. 2021, *A&A*, **648**, A103
- Duncan, D. K., Vaughan, A. H., Wilson, O. C., et al. 1991, *ApJS*, **76**, 383
- Eggen, O. J. 1984, *AJ*, **89**, 1358
- Eggen, O. J. 1989, *PASP*, **101**, 366
- Eisenbeiss, T., Ammler-von Eiff, M., Roell, T., et al. 2013, *A&A*, **556**, A53
- ESA 1997, The HIPPARCOS and Tycho catalogues. Astrometric and photometric star catalogues derived from the ESA HIPPARCOS Space Astrometry Mission, ESA Special Publication, 1200
- Flower, P. J. 1996, *ApJ*, **469**, 355
- Foreman-Mackey, D., Hogg, D. W., Lang, D., & Goodman, J. 2013, *PASP*, **125**, 306
- Francis, C., & Anderson, E. 2009, *New A*, **14**, 615
- Gagné, J., Mamajek, E. E., Malo, L., et al. 2018, *ApJ*, **856**, 23
- Gaia Collaboration 2018, VizieR Online Data Catalog: *I/345*
- Gaia Collaboration 2020, VizieR Online Data Catalog: *I/350*
- Giles, H. A. C., Collier Cameron, A., & Haywood, R. D. 2017, *MNRAS*, **472**, 1618
- Glebocki, R., & Gnacinski, P. 2005, VizieR Online Data Catalog: *III/244*
- González-Álvarez, E., Petralia, A., Micela, G., et al. 2021, *A&A*, **649**, A157
- Grankin, K. N. 2013, *Astron. Lett.*, **39**, 251
- Gray, D. F. 2008, *The Observation and Analysis of Stellar Photospheres* (Cambridge, UK: Cambridge University Press)
- Hall, J. C. 1996, *PASP*, **108**, 313
- Jayasinghe, T., Stanek, K. Z., Kochanek, C. S., et al. 2019, *MNRAS*, **485**, 961
- Jenkins, J. M., Twicken, J. D., McCauliff, S., et al. 2016, *SPIE Conf. Ser.*, **9913**, 99133E
- Jianke, L., & Collier Cameron, A. 1993, *MNRAS*, **261**, 766
- Johnson, D. R. H., & Soderblom, D. R. 1987, *AJ*, **93**, 864
- Jones, J., White, R. J., Boyajian, T., et al. 2015, *ApJ*, **813**, 58
- Kawaler, S. D. 1989, *ApJ*, **343**, L65
- Kenyon, S. J., & Hartmann, L. 1995, *ApJS*, **101**, 117
- Klutsch, A., Frasca, A., Guillout, P., et al. 2020, *A&A*, **637**, A43
- Kraft, R. P. 1967, *ApJ*, **150**, 551
- Lanza, A. F., Rodonò, M., & Pagano, I. 2004, *A&A*, **425**, 707
- Lanza, A. F., Das Chagas, M. L., & De Medeiros, J. R. 2014, *A&A*, **564**, A50
- López-Santiago, J., Montes, D., Gálvez-Ortiz, M. C., et al. 2010, *A&A*, **514**, A97
- Malavolta, L., Nascimbeni, V., Piotto, G., et al. 2016, *A&A*, **588**, A118
- Maldonado, J., Martínez-Arnáiz, R. M., Eiroa, C., Montes, D., & Montesinos, B. 2010, *A&A*, **521**, A12
- Maldonado, J., Phillips, D. F., Dumusque, X., et al. 2019, *A&A*, **627**, A118
- Maldonado, J., Petralia, A., Damasso, M., et al. 2021, *A&A*, **651**, A93
- Mamajek, E. E., & Hillenbrand, L. A. 2008, *ApJ*, **687**, 1264
- Mann, A. W., Johnson, M. C., Vanderburg, A., et al. 2020, *AJ*, **160**, 179
- Martínez-Arnáiz, R., Maldonado, J., Montes, D., Eiroa, C., & Montesinos, B. 2010, *A&A*, **520**, A79
- Martínez-Arnáiz, R., López-Santiago, J., Crespo-Chacón, I., & Montes, D. 2011a, *MNRAS*, **414**, 2629
- Martínez-Arnáiz, R., López-Santiago, J., Crespo-Chacón, I., & Montes, D. 2011b, *MNRAS*, **417**, 3100
- Mayor, M., Pepe, F., Queloz, D., et al. 2003, *The Messenger*, **114**, 20
- Messina, S., & Guinan, E. F. 2003, *A&A*, **409**, 1017
- Meunier, N., & Delfosse, X. 2009, *A&A*, **501**, 1103
- Montes, D., de Castro, E., Fernandez-Figueroa, M. J., & Cornide, M. 1995, *A&AS*, **114**, 287
- Montes, D., Fernández-Figueroa, M. J., De Castro, E., et al. 2000, *A&AS*, **146**, 103
- Montes, D., López-Santiago, J., Gálvez, M. C., et al. 2001, *MNRAS*, **328**, 45
- Montesinos, B., Thomas, J. H., Ventura, P., & Mazzitelli, I. 2001, *MNRAS*, **326**, 877
- Montesinos, B., Eiroa, C., Krivov, A. V., et al. 2016, *A&A*, **593**, A51
- Noyes, R. W., Hartmann, L. W., Baliunas, S. L., Duncan, D. K., & Vaughan, A. H. 1984, *ApJ*, **279**, 763
- Pecaut, M. J., & Mamajek, E. E. 2013, *ApJS*, **208**, 9
- Pecaut, M. J., & Mamajek, E. E. 2016, *MNRAS*, **461**, 794
- Santos, A. R. G., Mathur, S., García, R. A., Cunha, M. S., & Avelino, P. P. 2021, *MNRAS*, **508**, 267
- Scandariato, G., Maldonado, J., Affer, L., et al. 2017, *A&A*, **598**, A28
- Schatzman, E. 1962, *Ann. Astrophys.*, **25**, 18
- Schmitt, J. H. M. M., & Mittag, M. 2020, *Astron. Nachr.*, **341**, 497
- Shappee, B., Prieto, J., Stanek, K. Z., et al. 2014, in *AAS Meeting Abstracts*, 223, 236.03
- Silaj, J., & Landstreet, J. D. 2014, *A&A*, **566**, A132
- Skumanich, A. 1972, *ApJ*, **171**, 565
- Soderblom, D. R., Duncan, D. K., & Johnson, D. R. H. 1991, *ApJ*, **375**, 722
- Spada, F., Demarque, P., Kim, Y. C., & Sills, A. 2013, *ApJ*, **776**, 87
- Strassmeier, K. G., Granzer, T., Weber, M., et al. 2004, *Astron. Nachr.*, **325**, 527
- Suárez Mascareño, A., Rebolo, R., González Hernández, J. I., & Esposito, M. 2015, *MNRAS*, **452**, 2745
- Suárez Mascareño, A., Damasso, M., Lodieu, N., et al. 2021, *Nat. Astron.*, **6**, 232
- Torres, C. A. O., Quast, G. R., Melo, C. H. F., & Sterzik, M. F. 2008, *Young Nearby Loose Associations*, eds. B. Reipurth, 5, 757
- Wang, J., & Zhong, Z. 2018, *A&A*, **619**, L1
- Weber, E. J., & Davis, Leverett, J. 1967, *ApJ*, **148**, 217
- Zechmeister, M., & Kürster, M. 2009, *A&A*, **496**, 577

Appendix A: The (B-V) colour– T_{eff} relationship

In order to derive a relationship between effective temperature and (B-V) colour we used the data from Flower (1996, Table 3). The data were fitted to a seven-order polynomial fit of the form $(B - V) = a_0 + a_1 \times (\log T_{\text{eff}}) + a_2 \times (\log T_{\text{eff}})^2 + \dots + a_7 \times (\log T_{\text{eff}})^7$. Table A.1 gives the coefficients of the polynomial fit.

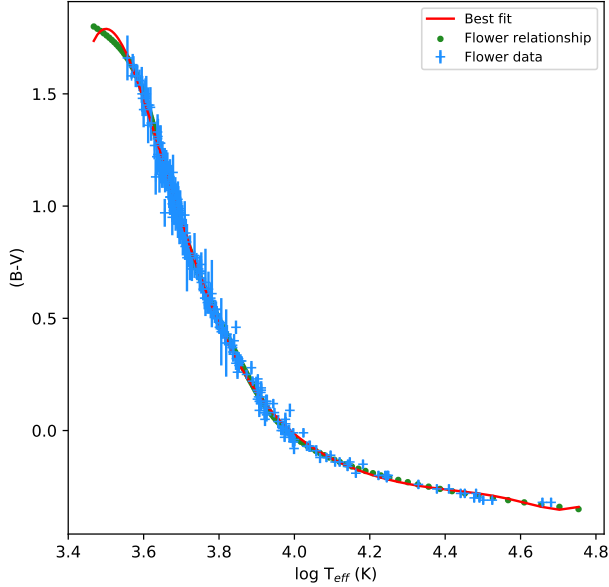


Fig. A.1: (B-V) vs. $\log T_{\text{eff}}$ relationship. The blue crosses show the data for the individual main sequence stars while the green dots corresponds to the colour– T_{eff} scale presented in Flower (1996). Our best fit is shown in red.

Table A.1: Coefficients of the (B-V) vs. $\log T_{\text{eff}}$ relationship.

Coefficient	Value
a_0	-6.5459×10^5
a_1	1.0991×10^6
a_2	-7.8965×10^5
a_3	3.1471×10^5
a_4	-7.5147×10^4
a_5	1.0752×10^4
a_6	-8.5347×10^2
a_7	2.8998×10^1

Appendix B: Online figures

Figure B.1 shows the pooled variance profile for all the stars with more than 20 observations.

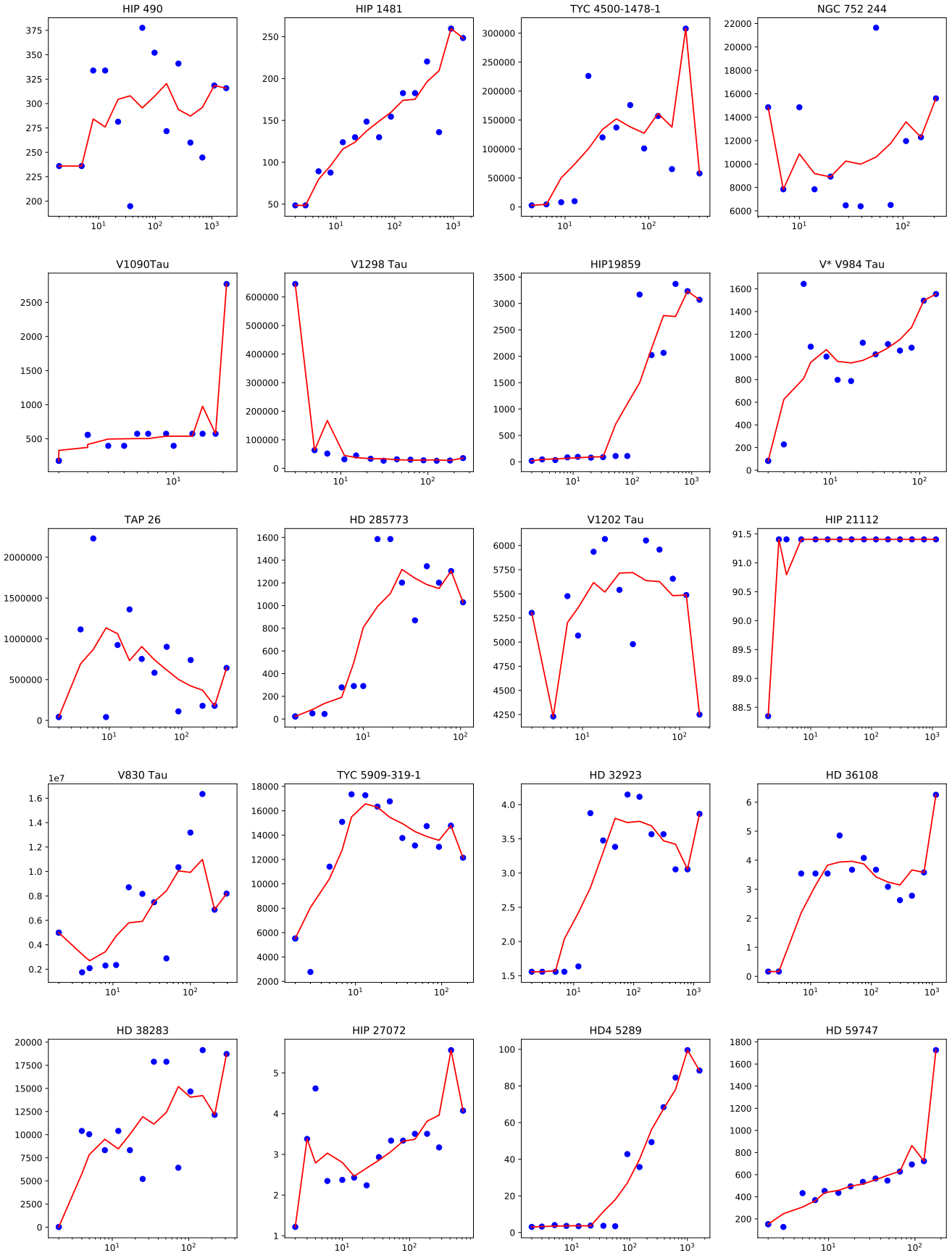


Fig. B.1: Pooled variance profile for stars with more than 20 observations. The red line is a smoothed function to improve the readability of the plots.

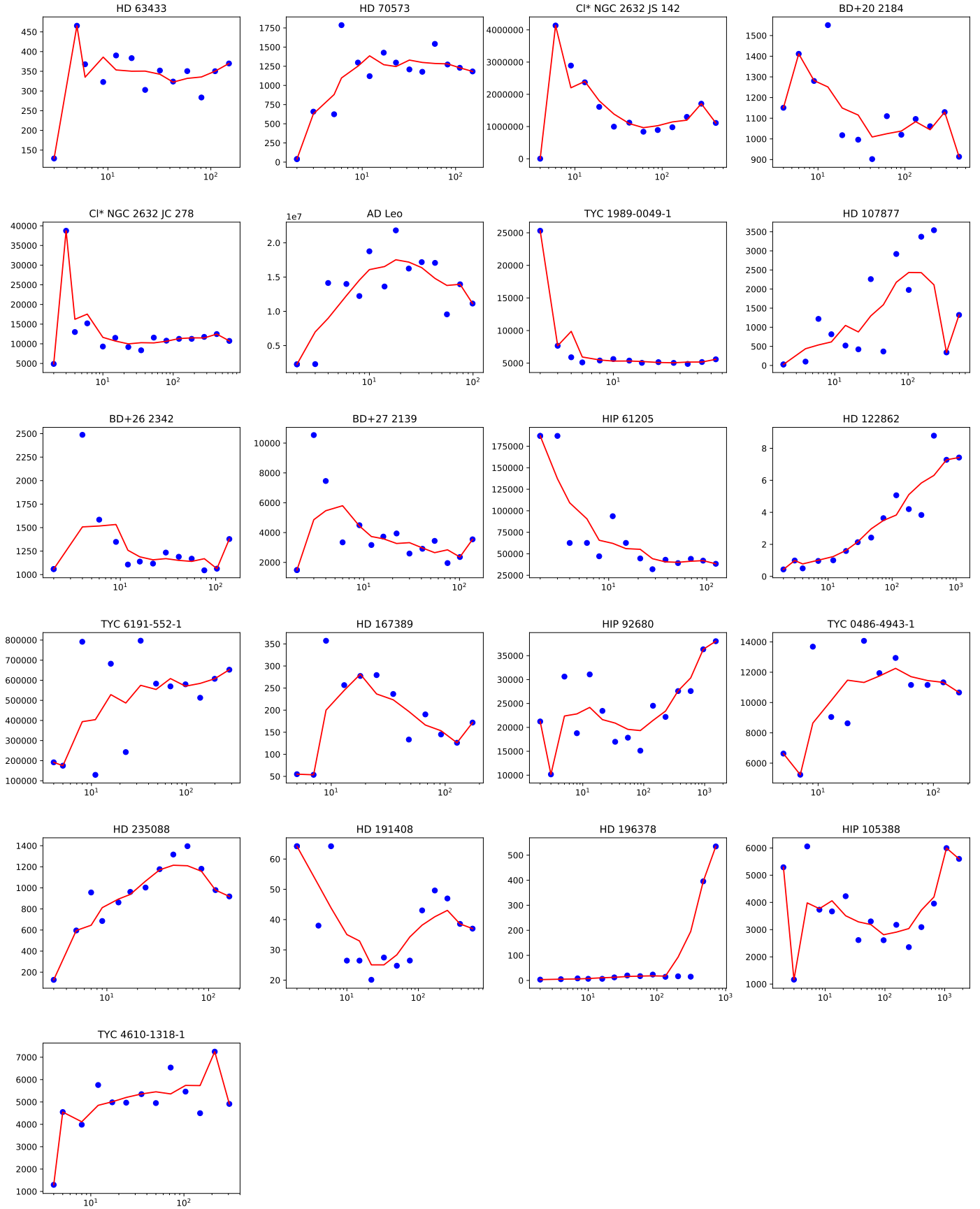


Fig. B.1: continued.

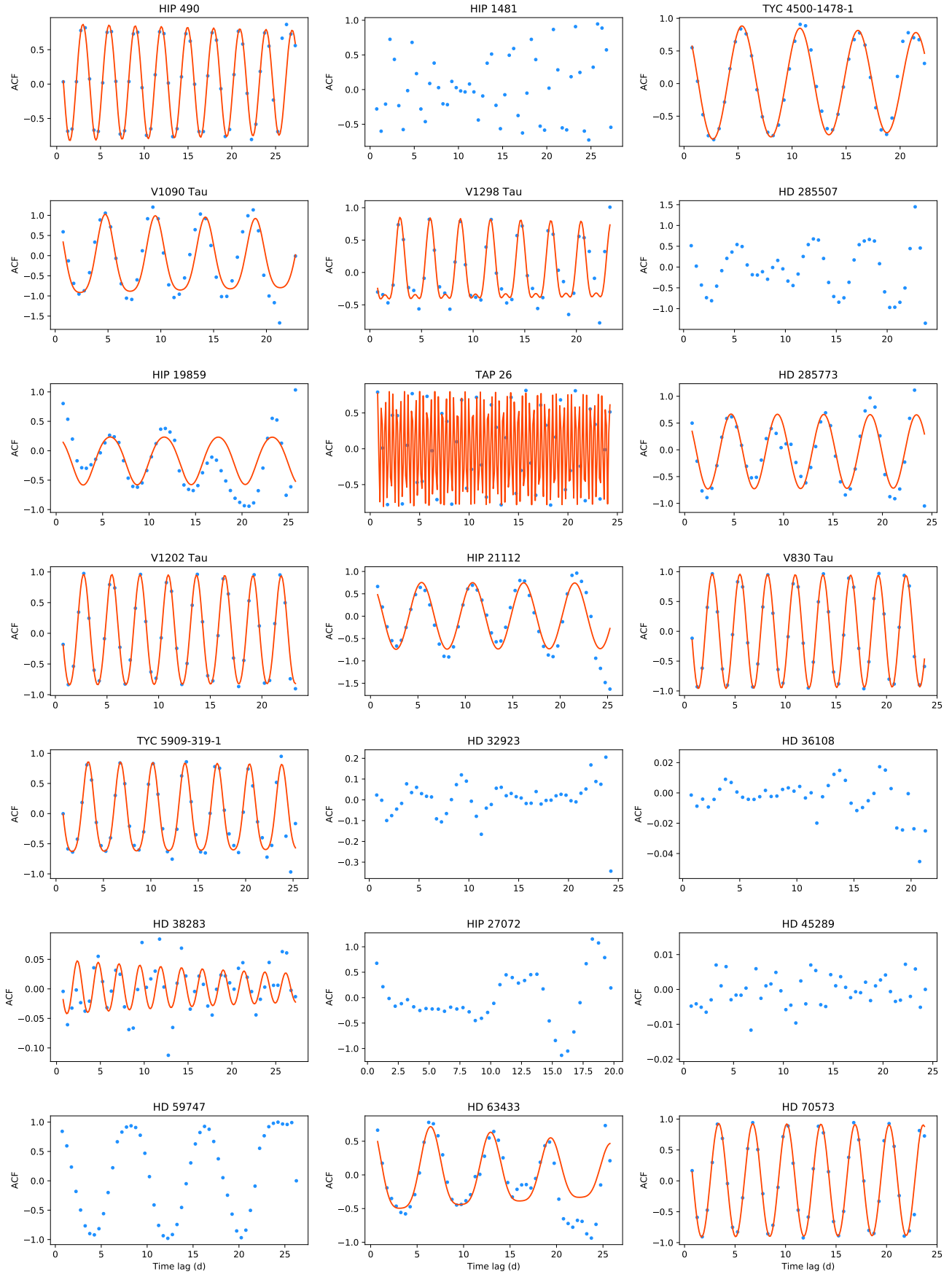


Fig. B.2: ACF curves of the TESS data. The red line shows the best fit.

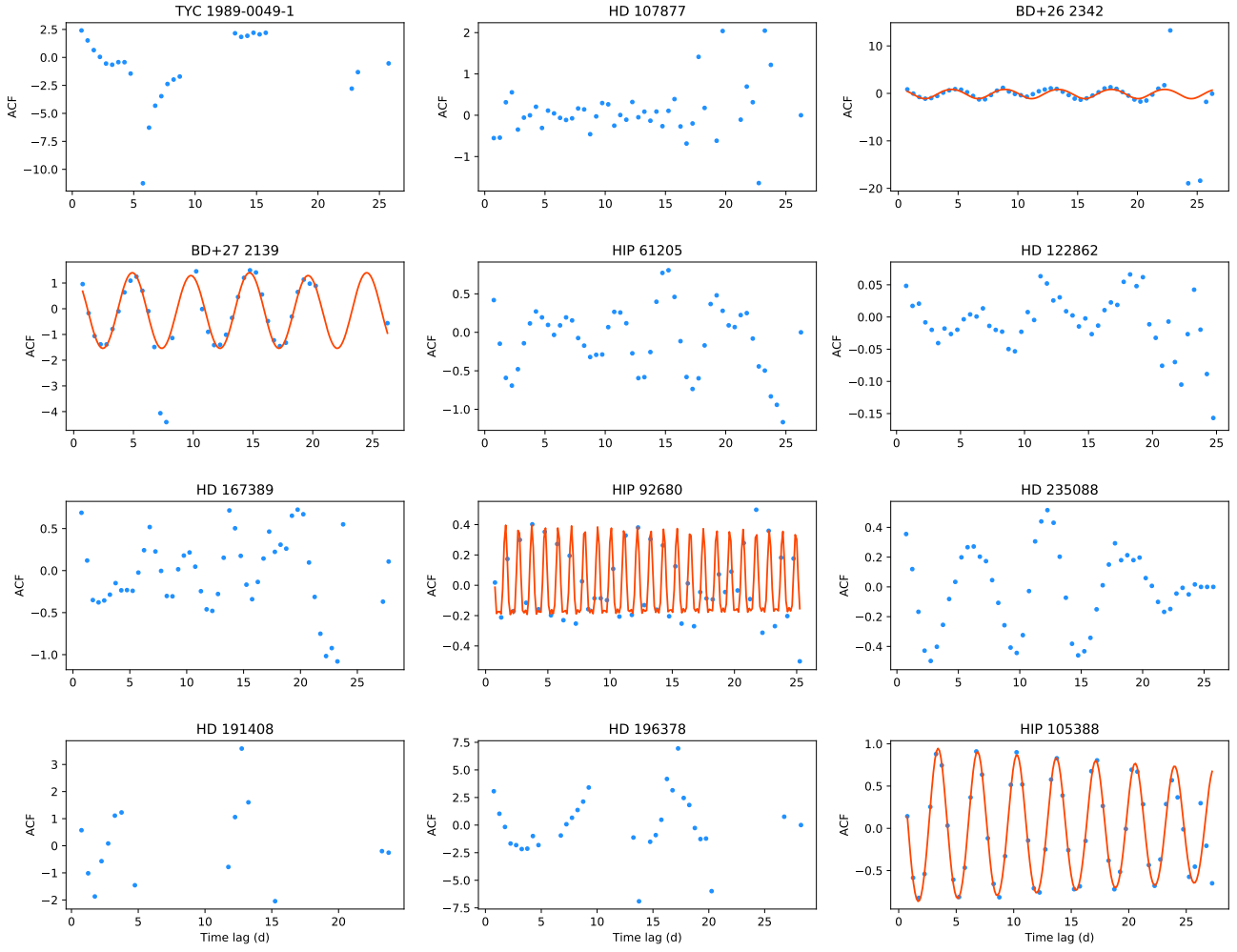


Fig. B.2: continued.

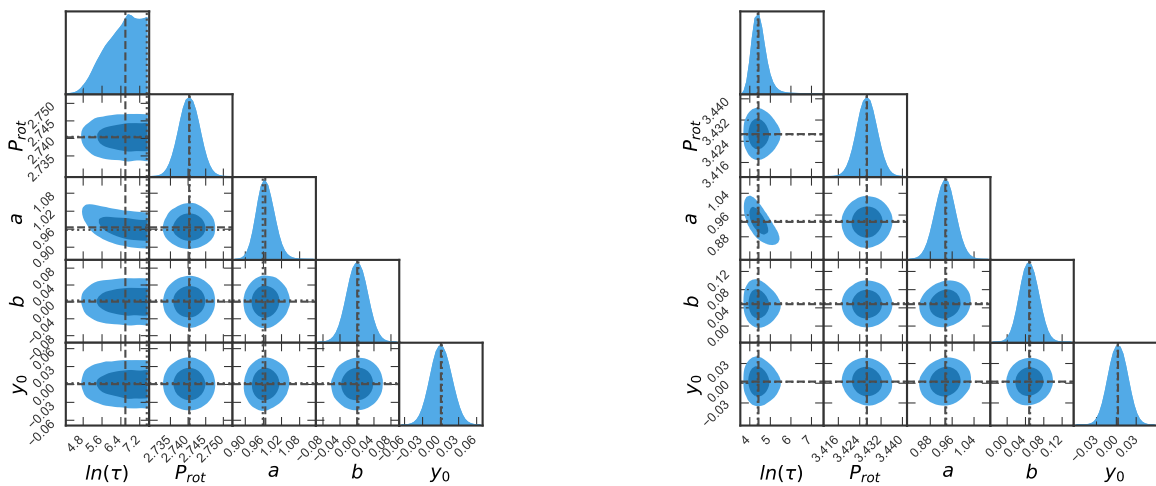


Fig. B.3: Posterior distribution of the ACF modelling for the star V830 Tau (left) and for the star HIP 105388 (right).

Appendix C: Online tables

Results produced in the framework of this work are only available at the CDS. Table C.1 provides the kinematic data of the stars analysed in this work. Namely, star identifier (column 1), galactic-spatial velocity components (columns 2, 3, and 4), preliminary young stellar group or association (column 5), best hypothesis and probability (columns 6 and 7) for stellar group or association membership obtained using the BANYAN tool (Gagné et al. 2018).

Table C.2 lists for each star (column 1) its corresponding age (column 2), effective temperature (column 3), (B-V) colour (column 4), $\log(R'_{\text{HK}})$ computed using the prescriptions given in Noyes et al. (1984) (column 5), projected rotational velocity, $v \sin i$, (column 6), stellar mass, radius, and luminosity (columns 7, 8, and 9; for simplicity, asymmetric uncertainties were averaged into a single error estimate), turnover convective timescale (column 10), number of observations (column 11), time span (column 12), and mean signal-to-noise ratio measured at ~ 550 nm. Table C.3 provides the emission excess in the Ca II H (column 2), Ca II K (column 3), and H α (column 4) lines.